Quantum Frontiers

上海交通大学
SHANGHAI JIAO TONG UNIVERSITY
李政道研究所
Tsung-Dao Lee Institute

ORIGINAL ARTICLE   **Open Access**

Chiral quantum phases and tricriticality in a Dicke triangle

Check for updates

Guo-Jing Cheng[1], Diego Fallas Padilla[2], Tao Deng[1], Yu-Yu Zhang[1*] and Han Pu[2*]

Abstract

The existence of quantum tricriticality and exotic phases are found in a tricritical Dicke triangle (TDT) where three cavities, each one containing an ensemble of three-level atoms, are connected to each other through the action of an artificial magnetic field. The conventional superradiant phase (SR) is connected to the normal phase through first- and second-order boundaries, with tricritical points located at the intersection of such boundaries. Apart from the SR phase, a chiral superradiant (CSR) phase is found by tuning the artificial magnetic field. This phase is characterized by a nonzero photon current and its boundary presents chiral tricritical points (CTCPs). Through the study of different critical exponents, we are able to differentiate the universality class of the CTCP and TCP from that of second-order critical points, as well as find distinctive critical behavior among the two different superradiant phases. The TDT can be implemented in various systems, including atoms in optical cavities as well as the circuit QED system, allowing the exploration of a great variety of critical manifolds.

Keywords: Dicke model, Quantum phase transition, Tricriticality

1 Introduction

Recent efforts have been devoted to exploring many-body quantum phases emerging in light-matter coupling systems using different platforms such as cavity and circuit QED [1–4], and cold atoms in optical lattices [5–7]. The rapid development of such platforms offers high control and tunability, allowing for the exploration of richer phase diagrams with more complex critical behaviors, for example, the study of tricritical points (TCPs) and higher-order critical points (multicritical points). TCPs were originally found in He^3-He^4 mixtures and a simple description of their mean-field characteristics can be done using the Landau theory of phase transitions [8]. These special points are located in the intersection of a second-order boundary and a first-order boundary, with both of them separating the same two phases [8–13]. Although well understood

from a theoretical perspective, quantum tricriticality is not abundant in real materials but can be found, for example, in certain metallic magnets [14–17].

Recently, light-matter interacting systems have been proposed to realize TCPs in experiments, specifically in generalizations of the Dicke model [12, 18]. The Dicke model has served historically as the cornerstone model in the description of the interaction of light with an ensemble of identical two-level atoms [19–22]. When the light-matter coupling strength is tuned above a critical threshold value, this system undergoes a superradiant phase transition, which has been realized in various experimental settings [23, 24].

Apart from interesting critical boundaries, atom-light interacting systems can be used to engineer exotic phases of matter when external fields are incorporated. Artificial magnetic fields have been used to explore chiral ground-state currents of interacting photons in a three-qubit loop [25], chiral phases in a quantum Rabi triangle [26], and fractional quantum Hall physics in the Jaynes-Cummings Hubbard lattice [27–29]. Advances in synthesizing such artificial magnetic fields have been reported

*Correspondence: yuyuzh@cqu.edu.cn; hpu@rice.edu
[1]Department of Physics, and Chongqing Key Laboratory for strongly coupled Physics, Chongqing University, Chongqing, 401330, China
[2]Department of Physics and Astronomy, and Rice Center for Quantum Materials, Rice University, Houston, TX, 77251, USA

in neutral ultracold atoms [30–32] and photonic systems [25, 33–36].

Here we propose a tricritical Dicke triangle (TDT) system as a building block for exploring all these features. The system is composed of three cavities each one containing an ensemble of three-level atoms allowing the realization of the tricritical Dicke Hamiltonian in each cavity. As a result, not only a second-order phase transition occurs, but also a first-order transition from the normal phase (NP) to the superradiant (SR) phase can be observed. The two types of phase boundaries meet at a conventional TCP. Interestingly, as photon hopping between neighboring cavities is permitted, new chiral superradiant phase (CSR) and chiral tricritical points (CTCP) can be found by tuning the artificial magnetic field, which breaks the $\mathbb{Z}_2$ and C_3 symmetries, causing a chiral current of photons in the ground state. Computation of the scaling exponents shows a plethora of critical behaviors, in particular, the CTCP and conventional TCPs are found to belong to different universality classes.

2 Single cavity tricritical Dicke model
Let us first consider a single cavity containing N identical three-level atoms coupled uniformly to the cavity mode. The Hamiltonian of this system is a generalization of the conventional Dicke model and reads

$$H_D = \omega a^\dagger a + \frac{\sqrt{2}g}{\sqrt{N}}\left(a^\dagger + a\right)\sum_{k=1}^{N} d^{(k)} + \Omega \sum_{k=1}^{N} h^{(k)}, \qquad (1)$$

where a ($a^\dagger$) is the photon annihilation (creation) operator of the single-mode cavity with frequency ω, g the atom-cavity coupling strength. The dipole operator $d^{(k)}$ of the k-th atom and the single-atom Hamiltonian $h^{(k)}$ are defined

as

$$d^{(k)} = \begin{pmatrix} 0 & 1 & 0 \\ 1 & 0 & \gamma \\ 0 & \gamma & 0 \end{pmatrix}, \qquad h^{(k)} = \begin{pmatrix} 1 & 0 & 0 \\ 0 & 0 & 0 \\ 0 & 0 & -1 \end{pmatrix}, \qquad (2)$$

where we have chosen the eigenstates of $h^{(k)}$ to be the basis states. These states are labelled as $|1\rangle$, $|0\rangle$ and $|-1\rangle$ as shown schematically in Fig. 1(a). The cavity field couples $|1\rangle$ and $|0\rangle$ as well as $|0\rangle$ and $|-1\rangle$, with the coupling strengths given by g and γg, respectively. The tunable dimensionless parameter γ serves as a control parameter.

The phase diagram can be described in terms of the scaled dimensionless coupling strength $\lambda = g/\sqrt{\Omega\omega}$ and the transition strength ratio γ as shown in Fig. 1(b). For simplicity, we set $\omega = \Omega = 1$. In the thermodynamic limit $N \to \infty$ the normal phase with $\langle a \rangle = 0$ and the superradiant phase with macroscopic photon population ($\langle a \rangle \propto \sqrt{N}$), are separated by first and second-order boundaries, indicated by the yellow dashed and the white solid lines in Fig. 1(b), respectively. These two types of boundaries meet at the tricritical point. A Landau theory approach can be followed to explore the expressions for the second- and first-order phase transitions, as well as for the TCP. Here, the order parameter is given by $\alpha = \langle a \rangle/\sqrt{N}$. In terms of this order-parameter, the mean-field energy is given by:

$$\frac{E_{\mathrm{MF}}}{\Omega N} = \frac{1}{8\lambda^2}\alpha^2 + \alpha d + h, \qquad (3)$$

where h and d are just the single atom operators given in Eq. (2), and the order parameter α has been rescaled by $\alpha \to \frac{2\sqrt{2}g}{\Omega}\alpha$. Due to the Z_2 symmetry of the Hamiltonian, the mean-field ground-state energy can be expanded as a
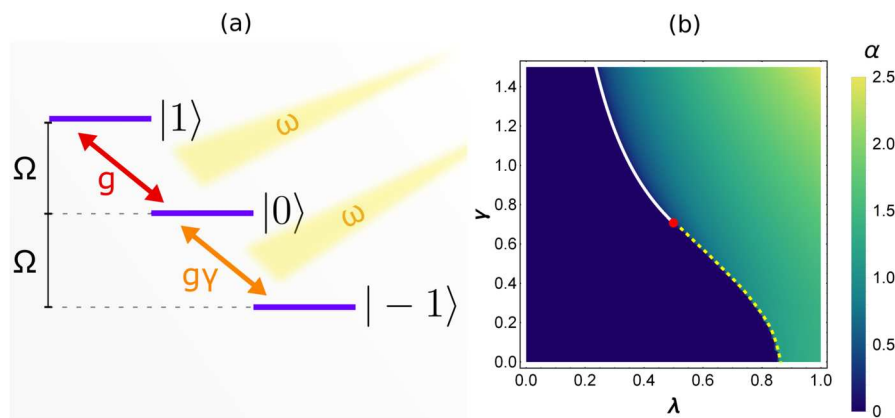

Figure 1 (**a**) Schematic showing the atomic levels of the tricritical Dicke model. Light with frequency ω couples the states $|1\rangle$ and $|0\rangle$ with interaction strength g, and the states $|0\rangle$ and $|-1\rangle$ with interaction strength $g\gamma$. (**b**) Phase diagram of the tricritical Dicke model in the λ-γ plane, using $\alpha = \langle a \rangle/\sqrt{N}$ as order parameter. The white solid line, yellow dashed line and red dot indicate the second-order boundary, first-order boundary, and tricritical point, respectively
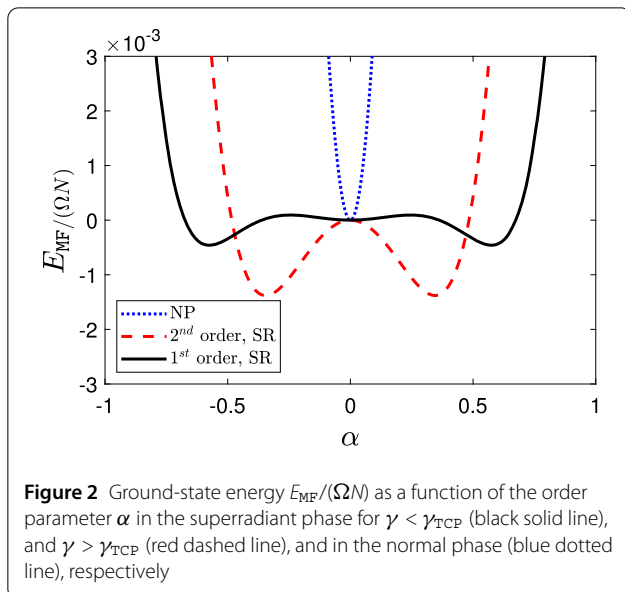
Taylor series in terms of α^2: $E_{MF} = \sum_{k=0}^{\infty} c_k \alpha^{2k}$. The coefficients c_k are obtained through perturbation theory, which is performed by treating h as the unperturbed Hamiltonian and d as the perturbation as shown in the Appendix and in Ref. [18]. Keeping the expansion up to order α^6 and discarding the constant term, the mean-field energy is approximated by

$$\frac{E_{MF}}{\Omega N} = c_1 \alpha^2 + c_2 \alpha^4 + c_3 \alpha^6, \tag{4}$$

where $c_1 = 1/(8\lambda^2) - \gamma^2$, $c_2 = \gamma^2(\gamma^2 - \frac{1}{2})$, and $c_3 = -\gamma^2(1 - 7\gamma^2 + 8\gamma^4)/4$ (see the Appendix). An ordinary 2nd-order critical point is obtained when $c_1 = 0$ and $c_2 > 0$, leading to the second-order boundary expression

$$\lambda_{2c}\gamma_{2c} = \frac{1}{\sqrt{8}}. \tag{5}$$

The tricritical point is defined by the condition $c_1 = c_2 = 0$ and $c_3 > 0$ [8, 18, 37]. For the single cavity case, the tricritical point is located at $\gamma_{TCP} = 1/\sqrt{2}$ and $\lambda_{TCP} = 1/2$. When $\gamma \geq \gamma_{TCP}$, one has $c_1 < 0$, and E_{MF} goes from having a single global minimum at $\alpha = 0$ for $\lambda < \lambda_{2c}$ to having two global minima at $\alpha_{\pm} = \pm\sqrt{(-c_2 + \sqrt{c_2^2 - 3c_1c_3})/3c_3}$ for $\lambda > \lambda_{2c}$, this behavior indicates the second-order character of the phase transition. In the case $\gamma < \gamma_{TCP}$, E_{MF} has three local minima at $\alpha_{\pm}$ and $\alpha = 0$, the global minimum switches from $\alpha = 0$ to $\alpha = \alpha_{\pm}$ as the phase transition is crossed, the discontinuous jump on the global minimum location characterizes the first-order boundary. The change in the order of the transition can be clearly observed in Fig. 2 where the ground-state energy E_{SR} as a function of α is presented for different values of γ and λ.

3 Tricritical Dicke triangle

We now consider three such cavity systems linked by photon hopping, as schematically shown in Fig. 3, forming the tricritical Dicke triangle (TDT). The TDT Hamiltonian is given by
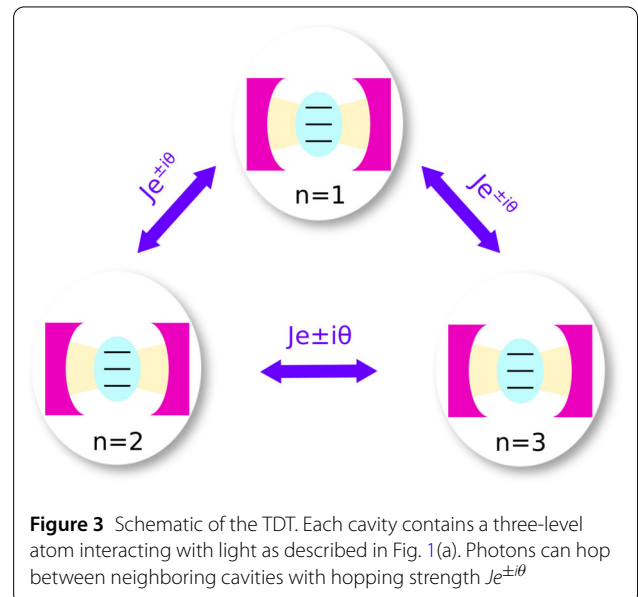
$$H = \sum_{n=1}^{3} H_{D,n} + \sum_{n=1}^{3} J\left(e^{i\theta} a_n^\dagger a_{n+1} + e^{-i\theta} a_{n+1}^\dagger a_n\right). \tag{6}$$

Here $H_{D,n}$ is the single-cavity Hamiltonian as given by Eq. (1), where we use the sub-index n to denote the nth cavity; J is the hopping amplitude between nearest-neighbor cavities with a phase θ. The complex photon hopping amplitude means that the photons are subjected to an artificial vector potential $A(r)$ such that $\theta = \int_{r_n}^{r_m} A(r)\,dr$ where r_n and r_m denote the position of the two neighboring cavities. Such an artificial vector potential or magnetic field can be achieved through temporal modulation of the photon-hopping strength on each cavity [26], and indeed has been experimentally implemented in a superconducting qubit platform [25]. Hence the TDT model we present here can be realized using existing technologies.

In analogy to the Dicke model, there exists a parity symmetry operator $P = \Pi_{i=1}^3 \exp\{i\pi[a_i^+ a_i + \sum_{k=1}^N (h^{(k)} + 1)]\}$, which satisfies $[H, P] = 0$ with eigenvalues ± 1. Besides such Z_2 symmetry, the Hamiltonian is real when $\theta = m\pi$ ($m \in \mathbb{Z}$), and, consequently, it preserves time-reversal symmetry (TRS). When this condition is not met, the breaking of the TRS can have important implications on the behavior of photons as will be shown later.

4 Normal phase of TDT

Let us first explore the normal phase (NP) of the TDT. This phase features no photon excitation just as in the single

Figure 2 Ground-state energy $E_{MF}/(\Omega N)$ as a function of the order parameter α in the superradiant phase for $\gamma < \gamma_{TCP}$ (black solid line), and $\gamma > \gamma_{TCP}$ (red dashed line), and in the normal phase (blue dotted line), respectively

Figure 3 Schematic of the TDT. Each cavity contains a three-level atom interacting with light as described in Fig. 1(a). Photons can hop between neighboring cavities with hopping strength $Je^{\pm i\theta}$

cavity case. We employ a Schrieffer-Wolff transformation $U_n = \exp(\sqrt{2}g/\sqrt{N}S_n)$ with an anti-Hermitian operator S_n given by

$$S_n = (a_n^\dagger + a_n)/\Omega \sum_{k=1}^{N} \begin{pmatrix} 0 & -1 & 0 \\ 1 & 0 & -\gamma \\ 0 & \gamma & 0 \end{pmatrix}, \qquad (7)$$

which makes the off-diagonal terms of the single-cavity Hamiltonian $H_{D,n}$ vanish. Neglecting higher-order terms in the thermodynamic limit $N \to \infty$, the transformed TDT Hamiltonian becomes

$$H_{\text{NP}} = \prod_{i=1}^{3} U_i^\dagger H \prod_{j=1}^{3} U_j$$

$$= \sum_{n=1}^{3} \left(\omega a_n^\dagger a_n + \Omega \sum_{k=1}^{N} h^{(k)} \right)$$

$$+ \sum_{n=1}^{3} J(e^{i\theta} a_n^\dagger a_{n+1} + H.c.)$$

$$+ \sum_{n=1}^{3} \frac{2g^2}{N\Omega} (a_n^\dagger + a_n)^2$$

$$\times \sum_{k=1}^{N} \begin{pmatrix} 1 & 0 & 0 \\ 0 & -1+\gamma^2 & 0 \\ 0 & 0 & -\gamma^2 \end{pmatrix}. \qquad (8)$$

The above Hamiltonian is diagonal in the atomic degrees of freedom, and an effective low-energy Hamiltonian can be found by projecting into the lowest energy state of the three-level atom,

$$H_{\text{NP}}^\downarrow = \sum_{n=1}^{3} \left(\omega - \frac{4g^2\gamma^2}{\Omega} \right) a_n^\dagger a_n - \frac{2g^2\gamma^2}{\Omega} (a_n^{\dagger 2} + a_n^2)$$

$$+ \sum_{n=1}^{3} J(e^{i\theta} a_n^\dagger a_{n+1} + e^{-i\theta} a_{n+1}^\dagger a_n) + E_0, \qquad (9)$$

where the energy constant is $E_0 = -6g^2\gamma^2/\Omega - 3N\Omega$.

Using the discrete Fourier transformation $a_n^\dagger = \sum_q a_q e^{\text{inq}}$ with the quasi-momentum $q = 0, \pm 2\pi/3$, we can rewrite the projected Hamiltonian $H_{\text{NP}}^\downarrow$ in momentum space as

$$H_{\text{NP}}^\downarrow = \sum_q \omega_q a_q^\dagger a_q - \frac{2g^2\gamma^2}{\Omega} (a_q^\dagger a_{-q}^\dagger + a_q a_{-q}) + E_0, \qquad (10)$$

where $\omega_q = \omega - 4g^2\gamma^2/\Omega + 2J\cos(\theta - q)$. By introducing a unitary transformation $S_q = \exp[\beta_q(a_q^\dagger a_{-q}^\dagger - a_q a_{-q})]$ with a variational squeezing parameter $\beta_q = -\frac{1}{8}\ln \frac{\omega_q + \omega_{-q} - 8g^2\gamma^2/\Omega}{\omega_q + \omega_{-q} + 8g^2\gamma^2/\Omega}$,

$H_{\text{NP}}^\downarrow$ can be diagonalized and takes the form $H_{\text{NP}}^\downarrow = \sum_q \varepsilon_q \times a_q^\dagger a_q + E_g$, where

$$E_g = E_0 + \frac{1}{2} \sum_q (\varepsilon_q - \omega_q) \qquad (11)$$

is the ground-state energy, and the excitation energies are given by

$$\varepsilon_q = \frac{1}{2} \left[\omega_q - \omega_{-q} + \sqrt{(\omega_q + \omega_{-q})^2 - 64g^4\gamma^4/\Omega^2} \right]. \qquad (12)$$

A second-order phase transition occurs when the gap between the first excited state and the ground state vanishes, then, the condition $\varepsilon_q = 0$ can be used to determine the location of these boundaries, leading to the critical values

$$\lambda_{2c}\gamma_{2c}$$

$$= \sqrt{\frac{1 + 4J/\omega\cos q\cos\theta + 4J^2/\omega^2\cos(\theta - q)\cos(\theta + q)}{8(1 + 2J/\omega\cos\theta\cos q)}}. \qquad (13)$$
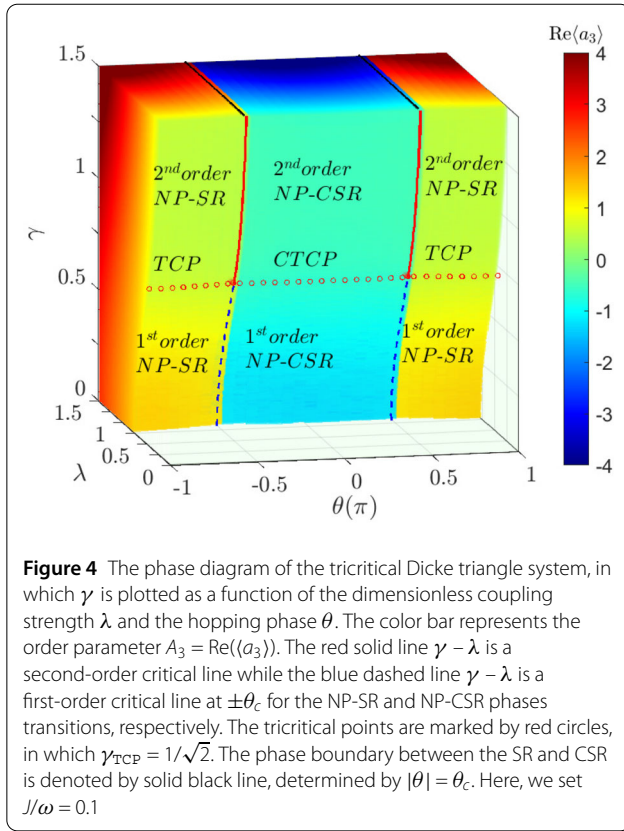
Note that if θ and J/ω are fixed, the expression above signals a γ-λ second-order line, but since θ will be taken as an additional control parameter that can vary, Eq. (13) refers, in general, to a second-order surface in the three dimensional parameter space spanned by γ, λ and θ, as shown in Fig. 4. Moreover, Eq. (13) describes two different second-order boundaries, one for $q = 0$ and the other for $q = \pm 2\pi/3$, as discussed in the following sections, each of these q-values is associated with a different superradiant phase. Additionally, note that Eq. (13) reduces to Eq. (5) for the single cavity case if we take the limit of no hopping between cavities $J = 0$, which is expected.

5 Superradiant phases of TDT

As the coupling strength increases to $\lambda > \lambda_{2c}$, the number of photons in each cavity becomes proportional to N. To capture the superradiant physics, the bosonic operators are shifted as $a_n \to \tilde{a}_n + \sqrt{N}\alpha_n$, $a_n^\dagger \to \tilde{a}_n^\dagger + \sqrt{N}\alpha_n^*$ with the complex displacement parameter $\alpha_n = A_n + iB_n$. Note that in the NP $\alpha_n = 0$. The transformed Hamiltonian becomes

$$H_{\text{SR}} = \sum_{n=1}^{3} \omega \tilde{a}_n^\dagger \tilde{a}_n + \sum_{k=1}^{N} \sqrt{\frac{2}{N}} g(\tilde{a}_n^\dagger + \tilde{a}_n)d^{(k)} + \Omega \sum_{k=1}^{N} h^{(k)}$$

$$+ \sum_{n=1}^{3} J\tilde{a}_n^\dagger(e^{i\theta}\tilde{a}_{n+1} + e^{-i\theta}\tilde{a}_{n-1}) + H_l + E_{\text{SR}}, \qquad (14)$$

where the linear term is $H_l = \sum_{n=1}^{3} \omega\sqrt{N}(\tilde{a}_n^\dagger \alpha_n + \tilde{a}_n \alpha_n^*) + \sqrt{N}J[\tilde{a}_n^\dagger(e^{i\theta}\alpha_{n+1} + e^{-i\theta}\alpha_{n-1}) + h.c.]$. The ground-state energy

Figure 4 The phase diagram of the tricritical Dicke triangle system, in which γ is plotted as a function of the dimensionless coupling strength λ and the hopping phase θ. The color bar represents the order parameter $A_3 = \mathrm{Re}(\langle a_3 \rangle)$. The red solid line $\gamma - \lambda$ is a second-order critical line while the blue dashed line $\gamma - \lambda$ is a first-order critical line at $\pm\theta_c$ for the NP-SR and NP-CSR phases transitions, respectively. The tricritical points are marked by red circles, in which $\gamma_{\mathrm{TCP}} = 1/\sqrt{2}$. The phase boundary between the SR and CSR is denoted by solid black line, determined by $|\theta| = \theta_c$. Here, we set $J/\omega = 0.1$

is expressed as

$$
\begin{aligned}
\frac{E_{\mathrm{SR}}}{N} = \sum_{n=1}^{3} & 2\sqrt{2}gA_n d + \Omega h + \omega\left(A_n^2 + B_n^2\right) \\
& + JA_n\big[\cos\theta(A_{n+1} + A_{n-1}) \\
& - \sin\theta(B_{n+1} - B_{n-1})\big] \\
& + JB_n\big[\cos\theta(B_{n+1} + B_{n-1}) \\
& + \sin\theta(A_{n+1} - A_{n-1})\big].
\end{aligned}
\tag{15}
$$

with d and h being the three-level operators in Eq. (2). The mean-field values A_n and B_n used to characterize the different phases are found by minimizing the energy given in Eq. (15), where two types of superradiant phases can be identified depending on whether $|\theta|$ is greater or lower than θ_c (see below). The complete phase diagram of the TDT is presented in Fig. 4. Note that although there are six order parameters, namely, A_n and B_n with $n = 1, 2, 3$, the value A_3 has been chosen to describe the phase diagram. Nonetheless, relations between all six-order parameters are provided in the following sections.

5.1 Conventional superradiant phase (SR)
In the SR phase $\alpha_n = A_n$ is real and non-zero, and is the same for all three cavities, $\alpha_n = \alpha_{n\pm1}$. Then, each cavity

behaves as an independent tricritical Dicke model. For a given value of θ, the boundary between the SR and NP phases is split into a second-order line (the red solid line) and a first-order critical line (the blue dashed line) as shown in Fig. 4. The two lines merge together in the TCP (represented with the red dots). In the three dimensional parameter space shown in Fig. 4, the TCPs form a line. The second-order phase boundary is consistent with the analytical expression γ_{2c}-λ_{2c} in Eq. (13) with the momentum $q = 0$.

Figure 5(a), (b) shows the order parameter α_n for the NP-SR phase transition as a function of λ. For a small value of the atomic transition ratio $\gamma = 0.1$, α_n is zero in the NP, and increases with an abrupt jump in the SR phase in Fig. 5(a), indicating a first-order phase transition. Since the transition between the middle and the upper state of the three-level atom dominates for a small γ, $\langle h_n \rangle > 0$ increases abruptly as well across the first-order transition (see the Appendix). However, for $\gamma = 1.5$ in Fig. 5(b), $\langle a_n \rangle$ changes smoothly from the NP to SR phase, exhibiting a second-order phase transition. Note that, in the SR, the ground state is two-fold degenerate as the configurations break the Z_2 symmetry. In Figs. 4 and 5, one of the degenerate configurations is chosen, the other one is simply obtained by changing the sign of the order parameter.

A perturbation theory analysis can be done in a similar fashion as for the single cavity case. Similarly, the mean-field energy for the SR can be approximated by

$$
\frac{E_{\mathrm{SR}}}{3\Omega N} = c_1\alpha^2 + c_2\alpha^4 + c_3\alpha^6,
\tag{16}
$$

with $c_1 = \frac{\omega'\Omega}{8g^2}$, where $\omega' = \omega + 2J\cos\theta$. c_2 and c_3 have the same form as in the single cavity case. Consequently, the second order boundary expression for the SR is given by

$$
\lambda_{2c}^{\mathrm{SR}}\gamma_{2c}^{\mathrm{SR}} = \frac{1}{2\sqrt{2}}\sqrt{1 + 2J/\omega\cos\theta},
\tag{17}
$$

which is consistent with Eq. (13) for $q = 0$. The tricritical point is located at $\gamma_{\mathrm{TCP}} = 1/\sqrt{2}$ and $\lambda_{\mathrm{TCP}} = \sqrt{1 + 2J/\omega\cos\theta}/2$. Note that, as expected, both of these results reduce to the single cavity case if the limit $J = 0$ is taken.

5.2 Chiral superradiant phase (CSR)
In the CSR phase, α_n is complex and depends on n. Minimization of the mean-field energy in Eq. (15) yields

$$
A_n \neq A_{n+1} = A_{n-1}, \qquad B_n = 0, \qquad B_{n+1} = B_{n-1}.
\tag{18}
$$

Since the solutions above break both the Z_2 and C_3 symmetries, the ground state in the CSR is six-fold degenerate. For a clear presentation of results we choose the particular solution $A_3 \neq A_1 = A_2$, $B_3 = 0$, $B_2 = -B_1$.
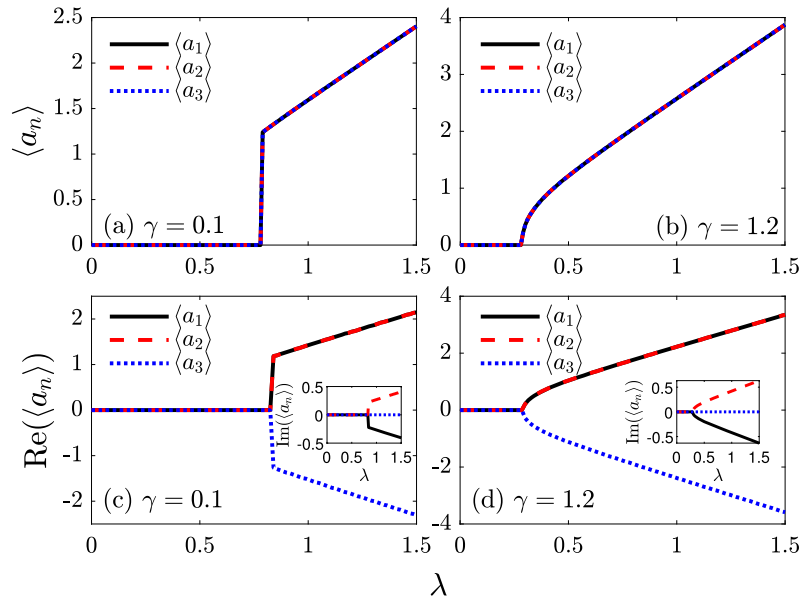
Figure 5 The order parameter $\langle a_n \rangle = \alpha_n$ as a function of the dimensionless coupling strength λ across the NP-SR phase transition of (**a**) first-order $\gamma = 0.1$, and (**b**) second-order $\gamma = 1.5$. θ is kept fixed at $2\pi/3 > \theta_c$. The real part of $\langle a_n \rangle$ across the NP-CSR phase transition of (**c**) first-order $\gamma = 0.1$, and (**d**) second-order $\gamma = 1.5$. θ is kept fixed at $\pi/3 < \theta_c$. The inset corresponds to the imaginary part $B_n = \text{Im}(\langle a_n \rangle)$ of the order parameter

In Fig. 5(c), (d) the order parameter α_n is shown for the CSR phase transition. As observed in both panels, the order parameter is site-dependent, contrary to the SR case. However, there is still a change in the order of the transition depending on the γ value. Consequently, just as in the SR phase, there are chiral tricritical points (CTCPs) in the CSR phase as observed in Fig. 4.

To investigate the phase boundaries in the CSR phase, we start with a particular solution $A_3 = A$, $A_1 = A_2 = \widetilde{A}$ and $B_3 = 0$. Similar to the SR case, the mean-field ground-state energy can be written as a Taylor series in terms of A^2 and $\widetilde{A}^2$

$$\frac{E_{\text{CSR}}}{\Omega N} = 2\big(\omega_{\text{CSR}} + J' - \gamma^2\big)\widetilde{A}^2 + \big(\omega_{\text{CSR}} - \gamma^2\big)A^2$$
$$+ 4J'A\widetilde{A} + c_2\big(A^4 + 2\widetilde{A}^4\big), \qquad (19)$$

where $\omega_{\text{CSR}} = [\omega - 2J^2 \sin^2\theta/(\omega - J\cos\theta)]\Omega/8g^2$, $J' = \Omega/8g^2(J\cos\theta + \frac{J^2 \sin^2\theta}{\omega - J\cos\theta})$ and the coefficient $c_2 = \gamma^2(\gamma^2 - \frac{1}{2})$. By minimizing the energy using $\partial E/\partial A = 0$ and $\partial E/\partial \widetilde{A} = 0$, the expression for the second-order boundary in the CSR can be found to be

$$\lambda_{2c}^{\text{CSR}}\gamma_{2c}^{\text{CSR}}$$
$$= \frac{1}{2\sqrt{2}}\sqrt{\frac{1 - 2J/\omega\cos\theta + J^2/\omega^2(\cos^2\theta - 3\sin^2\theta)}{1 - J/\omega\cos\theta}},$$
$$(20)$$

which is consistent with Eq. (13) when choosing $q = \pm 2\pi/3$. As expected, the critical line γ-λ of the second-order NP-CSR transition in Fig. 4 fits well with the analytical solutions $\lambda_{2c}^{\text{CSR}}$. The CTCP is located at $\gamma_{\text{CTCP}} = 1/\sqrt{2}$ as a consequence of setting $c_2 = 0$ in Eq.(19). By substituting γ_{CTCP} into Eq. (20), λ_{CTCP} can be determined.

If γ and λ are fixed inside the SR phase, and θ is varied until entering the CSR the order parameter changes discontinuously. Thus, the phase transition between the two superradiant phases is of first-order and indicated by the solid black line in Fig. 4. Right at the boundary between the SR and CSR phases, conditions $B_n = 0$ and $A_{n-1} = A_{n+1} = \pm A_n$ need to be satisfied. From Eq. (15), this implies $J\cos\theta + J^2 \sin^2\theta/(\omega - J\cos\theta) = 0$, which leads to the critical hopping phase that separates the SR and CSR

$$\theta_c = \cos^{-1}\left(-\frac{2J}{\sqrt{8J^2 + \omega^2} + \omega}\right). \qquad (21)$$

The entire superradiance region is split into the CSR phase regime for $|\theta| \leq \theta_c$ and the SR phase regime for $|\theta| > \theta_c$.

To characterize further the chirality in the CSR phase, we analyze the ground-state current of photons in the closed loop of three cavities. Similar to the continuity equation in classical systems, the photon current operator can be explicitly defined as

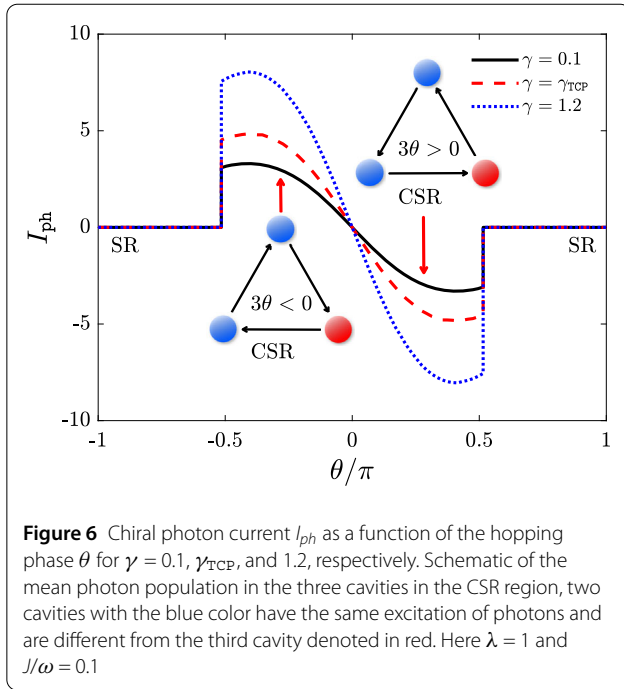$$I_{\text{ph}} = i\big[\big(a_1^\dagger a_2 + a_2^\dagger a_3 + a_3^\dagger a_1\big) - h.c.\big]. \qquad (22)$$

Figure 6 Chiral photon current I_{ph} as a function of the hopping phase θ for $\gamma = 0.1$, γ_{TCP}, and 1.2, respectively. Schematic of the mean photon population in the three cavities in the CSR region, two cavities with the blue color have the same excitation of photons and are different from the third cavity denoted in red. Here $\lambda = 1$ and $J/\omega = 0.1$

Figure 6 shows the photon current in the ground state for $\lambda > \lambda_{2c}$ in the SR and CSR phases. By varying the effective magnetic flux θ, a discontinuous jump of I_{ph} is observed at the critical hopping phase $\pm\theta_c$. I_{ph} goes from zero in the SR phase, to a non-zero value in the CSR phase and changes its sign depending on the phase θ. Then, varying θ changes the orientation of the photons circulating in the loop from clockwise to anticlockwise, a signature of the chiral phase. The ground-state current of photons is associated with the nonuniform excitation of photons in three cavities, which is induced by the magnetic flux.

6 Critical behavior

Second-order phase transitions are characterized by their scaling exponents in the vicinity of the transition. Here, we explore the critical behavior of the total photon number $N_{\text{ph}} = \sum_{n=1}^{3} \langle a_n^\dagger a_n \rangle$ near three important regions: the second-order critical boundary, the TCP and the CTCP, in order to classify the universality of each of these critical manifolds.

First, we consider a point (γ, λ) in the SR region and close to the second-order critical line for fixed $\theta = 2\pi/3$. A line through this point is perpendicular to the critical line and intercepts the critical line at a second-order critical point $(\gamma_{2c}^{\text{SR}}, \lambda_{2c}^{\text{SR}})$ [12]. Around the critical point, the photon number scales like $N_{\text{ph}} \propto L^\beta$, where $L \equiv \sqrt{(\lambda - \lambda_{2c}^{\text{SR}})^2 + (\gamma - \gamma_{2c}^{\text{SR}})^2}$ is the distance between the point and the second-order critical point. Figure 7(a) displays N_{ph} at (γ, λ) as a function of L. The critical exponent for this transition is $\beta = 1$, consequently, $N_{\text{ph}}^{\text{2nd}} \propto L$. However,

if the perpendicular line through (γ, λ) intercepts the critical line at the TCP $(\gamma_{\text{TCP}}, \lambda_{\text{TCP}})$, one has a different scaling

$$N_{\text{ph}}^{\text{TCP}} \propto L^{1/2} \tag{23}$$

which gives a critical exponent 1/2 for the TCP. This illustrates that the TCP belongs to a different universality class in comparison to the conventional second-order critical points.

Figure 7(b) show the scaling behaviors for the CSR phase at $\theta = \pi/3$. The mean photon number in one of the sites is different from that in the other two cavities due to the break of the C_3 symmetry. However, we found that the photon number in each cavity has the same scaling behavior. Similar to the SR phase, the critical exponent for the 2nd-order critical point $(\gamma_{2c}^{\text{CSR}}, \lambda_{2c}^{\text{CSR}})$ is obtained to be 1. The scaling function at the CTCP $(\gamma_{\text{CTCP}}, \lambda_{\text{CTCP}})$ is found to be

$$N_{\text{ph}}^{\text{CTCP}} \propto L^{1/2}. \tag{24}$$

This indicates that all tricritical points, regardless of whether they are TCP or CTCP, have the same scaling exponent for photon numbers.

Finally, Fig. 7(c) shows the scaling exponents at $\theta = \theta_c$ at the critical line. This line is special since it represents the line of triple points at which three phases (SR, CSR, and NP) coexist. The scaling along this line shows the same behavior, which is expected, as both SR and CSR have the same scaling exponents.

The exponent of N_{ph} (β) is useful to distinguish between ordinary critical points and tricritical ones, nonetheless, it does not signal any differences between the SR and CSR phase transitions, which is unexpected as both phases have very distinct features, the scaling behavior of other quantities could be useful for further characterization of the critical behavior. To this end, let us examine other critical exponents such as the scaling of the excitation energy. The effective low-energy Hamiltonian in Eq. (9) has a quadratic form in the a_n operators, consequently, a Bogoliubov transformation can be performed to diagonalize the Hamiltonian in the form

$$H_{\text{NP}}^\downarrow = \sum_q \varepsilon_q a_q^\dagger a_q + E_g, \tag{25}$$

with $q = 0, \pm 2\pi/3$, E_g being the ground state energy given in Eq. (11), ε_q being the excitation energies given in Eq. (12), and a_q ($a_q^\dagger$) being a new set of annihilation (creation) operators obtained through the Bogoliubov transformation. Precisely at the critical points, the lowest of the set of excitation energies $\{\varepsilon_q\}$ vanishes, and we denote the lowest excitation energy by ε_1. consequently, we expect that around the critical point this quantity behaves as $\varepsilon_1 \propto L^\eta$.
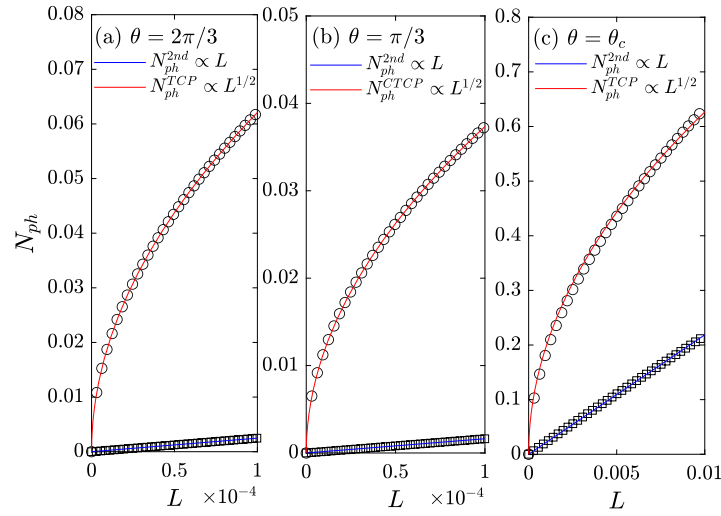
Figure 7 Mean photons in three cavities N_{ph} as a function of the distance L between a point inside the corresponding superradiant phase and a critical point located in the boundary with the normal phase for the CSR phase (**a**), the SR phase (**b**), and a triple point (**c**). Conventional second-order critical points ($\gamma = 0.9$) are represented by open squares, while TCP's and CTCP's are represented with open circles. The corresponding fitting lines are listed. Here $J/\omega = 0.1$
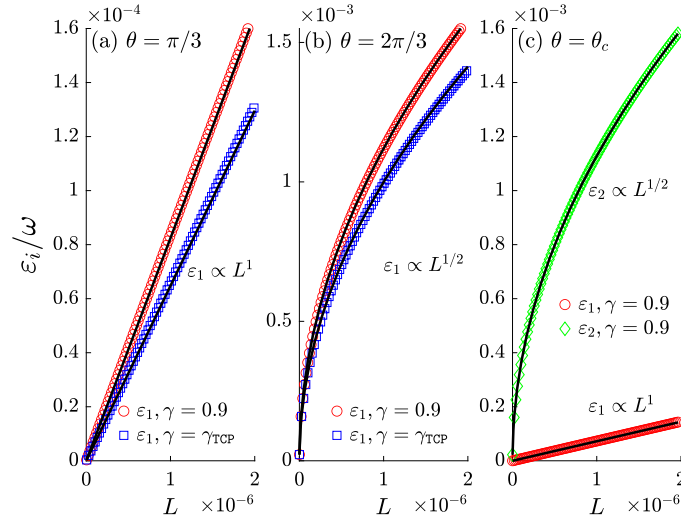

Figure 8 Excitation energies ε_i as a function of the distance L between a point in the normal phase and critical point located in the boundary with the CSR phase (**a**), the SR phase (**b**), or a triple point (**c**). ε_1 denotes the lowest excitation energy, and ε_2 is the second-lowest. Both conventional second-order critical points ($\gamma = 0.9$) and tricritical points (TCP's and CTCP's) with $\gamma = \gamma_{TCP}$ are explored. The fitting lines are shown on each panel. Here, $J/\omega = 0.01$

Since Eq. (25) is only valid in the normal phase, L in this case is the distance between a point in the normal phase and the critical point. In Fig. 8, the scaling of ε_1 as a function of L is shown for both the SR and CSR phases. In the SR we find that $\varepsilon_1 = \varepsilon_{q=0}$, while in the CSR $\varepsilon_1 = \varepsilon_{q=\pm 2\pi/3}$. The exponent η is found to be 1 for the CSR while it has a value of 1/2 for the SR. This means that the excitation behavior on the onset of the phase boundaries is different be-

tween such phases. However, this exponent does not seem to be sensitive to the order of the critical point as tricritical points follow the same behavior as conventional critical points.

Moreover, we note that at a triple point ($\theta = \theta_c$) two excitation energies vanish (denoted by ε_1 and ε_2) instead of just one, as a sign of the coexistence of both superradiant phases at this point This behavior is illustrated in Fig. 8(c).

Table 1 Critical exponents β and η for each critical boundary/point

Critical boundary/point	β	η
SR-NP second-order boundary	1	1/2
Tricritical points (TCP)	1/2	1/2
CSR-NP second-order boundary	1	1
Chiral tricritical points (CTCP)	1/2	1
Second order critical points at the triple line	1	1/2 & 1
Tricritical points at the triple line	1/2	1/2 & 1

Consistently, the two η exponents are found to be 1/2 and 1 representing the SR and CSR phase transitions, respectively. A summary of the critical exponents for each critical boundary/point is presented in Table 1.

A study of ε_1 for points inside the superradiant region could retrieve some interesting behavior as described in Refs. [38, 39]. However, an effective Hamiltonian of the form of Eq. (9) is not easily obtainable for the TDT in the superradiant regions. Nonetheless, it seems that the complementary use of η and β exponents already allow us to characterize the critical behavior of the different points and boundaries in the system, illustrating the great variety of features that can be explored using the TDT.

7 Conclusion

A different transition ratio between atomic levels and the incorporation of an artificial magnetic field make the tricritical Dicke triangle an ideal platform for studying the interplay between higher-order critical points and chiral phases of matter. Two different superradiant phases can be found by tuning the phase θ of the photon hopping amplitude, and both of them can be accessed from the normal phase through first- and second-order transitions, as well as tricritical points. The scaling behavior of the excitation energy indicates that the NP-SR and the NP-CSR transitions belong to different universality classes; while the scaling behavior of the photon mean-field population elucidates a different universality between tricritical and ordinary critical points, making evident the richness of critical manifolds in the system. Our study opens intriguing avenues for exploring quantum tricriticality and rich phases in a single light-matter interacting platform.

Finally, we want to comment that two natural extensions of the current work can be explored in the future. (1) We may consider, instead of three-level atoms, general multi-level atoms. Such a system can support multicritical points [18]. In general, more atomic levels can support higher-order critical points. (2) Instead of three cavities on a ring, we can consider an even number of cavities. Recent work has shown that there exist some qualitative differences between odd and even number of cavities, as the former exhibiting geometric frustration [38, 39].

Appendix: Coefficients c_k's by perturbation theory

We apply perturbation theory to obtain the coefficients c_k's in Eq. (16). The mean-field Hamiltonian in the SR phase is given by

$$\frac{E_{SR}}{3N\Omega} = \frac{\omega + 2J\cos\theta}{\Omega}\alpha^2 + H_a, \tag{A1}$$

$$H_a = D + h. \tag{A2}$$

with $\alpha' = 2\sqrt{2}g\alpha/\Omega$ and $D = \alpha'd$. h is treated as the unperturbed Hamiltonian, which gives the eigenstates $|\varepsilon_i\rangle$ ($i = 1, 2, 3$) with the eigenvalues $\varepsilon_1 = -1$, $\varepsilon_2 = 0$ and $\varepsilon_3 = 1$. And d is the perturbation term, the coefficients c_k are obtained by the perturbation expansion up to $(2k)$ order. The ground-state wave function can be expanded as

$$|\varphi\rangle = |\varepsilon_1\rangle + \sum_{m\neq 1}\frac{|m\rangle\langle m|}{E - \varepsilon_m}D|\varphi\rangle$$

$$= |\varepsilon_1\rangle + G(E)D|\varphi\rangle, \tag{A3}$$

where $G(E) = \sum_{m\neq 1}|m\rangle\langle m|/(E - \varepsilon_m)$ and $H_a|\varphi\rangle = E|\varphi\rangle$. This means that the wave function can be found through iteration as:

$$|\varphi\rangle = |\varepsilon_1\rangle + G(E)D|n\rangle + G(E)DG(E)D|n\rangle$$

$$+ G(E)DG(E)DG(E)D|n\rangle + \cdots \tag{A4}$$

From $D|\varphi\rangle = (E - \varepsilon_1)|\varphi\rangle$, we obtain the ground-state energy

$$E - \varepsilon_1 = \langle\varepsilon_1|D|\varphi\rangle. \tag{A5}$$

By substituting the wave function into the equation above, the ground-state energy is given by

$$E = \varepsilon_1 + \langle\varepsilon_1|D|\varepsilon_1\rangle + \langle\varepsilon_1|DG(E)D|\varepsilon_1\rangle$$

$$+ \langle\varepsilon_1|DG(E)DG(E)D|\varepsilon_1\rangle + \cdots \tag{A6}$$

Clearly, the zero-th energy correction is $E^{(0)} = \varepsilon_1$. Since $\langle\varepsilon_1|D|\varepsilon_1\rangle$ is zero due to the symmetry of the Hamiltonian, the first non-zero correction is the second-order one

$$E^{(2)} = \varepsilon_1 + \langle\varepsilon_1|DG(E)D|\varepsilon_1\rangle$$

$$= \varepsilon_1 + \frac{|D_{12}|^2}{E^{(0)} - \varepsilon_2} = -1 - \alpha'^2\gamma^2. \tag{A7}$$

The fourth-order correction of the ground-state energy is

$$E^{(4)} = \varepsilon_1 + \langle\varepsilon_1|DG(E)D|\varepsilon_1\rangle$$

$$+ \langle\varepsilon_1|DG(E)DG(E)DG(E)D|\varepsilon_1\rangle$$

$$= \varepsilon_1 + \alpha'^2\frac{|d_{12}|^2}{E^{(2)} - \varepsilon_2}$$

$$+ \alpha'^4 \sum_{m \neq 1} \sum_{n \neq 1} \sum_{k \neq 1} \langle \varepsilon_1 | d \frac{|m\rangle\langle m|}{E^{(0)} - \varepsilon_m} d \frac{|n\rangle\langle n|}{E^{(0)} - \varepsilon_n}$$

$$\times d \frac{|k\rangle\langle k|}{E^{(0)} - \varepsilon_k} d | \varepsilon_1 \rangle$$

$$= -1 + \frac{\alpha'^2 \gamma^2}{-1 - \alpha'^2 \gamma^2} - \frac{1}{2} \alpha'^4 \gamma^2. \tag{A8}$$

Since α is small around the critical point, the above energy can be approximated by

$$E^{(4)} = -1 - \alpha'^2 \gamma^2 + \gamma^2 \left(\gamma^2 - \frac{1}{2} \right) \alpha'^4. \tag{A9}$$

The sixth-order correction of the energy is given by

$$E^{(6)} = \varepsilon_1 + \langle \varepsilon_1 | DG(E)D | \varepsilon_1 \rangle$$

$$+ \langle \varepsilon_1 | DG(E)DG(E)DG(E)D | \varepsilon_1 \rangle$$

$$+ \langle \varepsilon_1 | DG(E)DG(E)DG(E)DG(E)DG(E)D | \varepsilon_1 \rangle$$

$$= \varepsilon_1 + \alpha'^2 \frac{|d_{12}|^2}{E^{(4)} - \varepsilon_2}$$

$$+ \alpha'^4 \sum_{m \neq 1} \sum_{n \neq 1} \sum_{k \neq 1} \langle \varepsilon_1 | d \frac{|m\rangle\langle m|}{E^{(2)} - \varepsilon_m} d \frac{|n\rangle\langle n|}{E^{(2)} - \varepsilon_n}$$

$$\times d \frac{|k\rangle\langle k|}{E^{(2)} - \varepsilon_k} d | \varepsilon_1 \rangle$$

$$+ \alpha'^6 \sum_{m \neq 1} \sum_{n \neq 1} \sum_{k \neq 1} \sum_{i \neq 1} \sum_{j \neq 1} \frac{\langle \varepsilon_1 | m \rangle d_{mn}}{E^{(0)} - \varepsilon_m} \frac{d_{nk}}{E^{(0)} - \varepsilon_n}$$

$$\times \frac{d_{ki}}{E^{(0)} - \varepsilon_k} \frac{d_{ij}}{E^{(0)} - \varepsilon_i} \frac{\langle j | \varepsilon_1 \rangle}{E^{(0)} - \varepsilon_j}$$

$$= \varepsilon_1 + \frac{\alpha'^2 \gamma^2}{E^{(4)} - \varepsilon_2} + \alpha'^4 \frac{|d_{12}|^2}{(E^{(2)} - \varepsilon_2)^2} \frac{|d_{23}|^2}{E^{(2)} - \varepsilon_3}$$

$$+ \alpha'^6 \frac{|d_{12}|^3}{(E^{(0)} - \varepsilon_2)^3} \frac{|d_{23}|^3}{(E^{(0)} - \varepsilon_3)^2}. \tag{A10}$$

Then, the ground-state energy up to the sixth-order in perturbation can be approximately given as a power series in terms of α^2

$$E^{(6)} = -1 - \alpha'^2 \gamma^2 + \gamma^2 \left(\gamma^2 - \frac{1}{2} \right) \alpha'^4$$

$$- \frac{1}{4} \gamma^2 \left(8\gamma^4 - 7\gamma^2 + 1 \right) \alpha'^6. \tag{A11}$$

The expected value of $\langle h_n \rangle$ for a single atom in the n-th cavity is calculated by minimizing the energy in Eq. (A1). Figure A1 shows $\langle h_n \rangle$ in the three cavities for the first- and second-order phase transitions from the NP to SR and CSR phases. In the NP phase, the atom stays in the down state with $\langle h_n \rangle = -1$. For the first-order phase transition (panels (a) and (c)), $\langle h_n \rangle$ exhibits an abrupt jump from -1 to $\langle h_n \rangle > 0$. In contrast, $\langle h_n \rangle$ increases smoothly from -1 across the second-order phase transition with $\gamma = 1.5$ as show in panels (b) and (d).
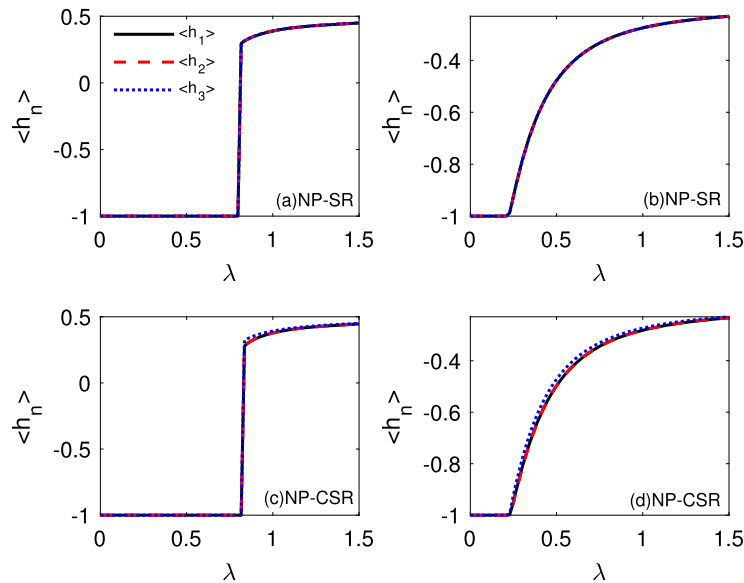

Figure A1 $\langle h_n \rangle$ of a single atom in the n-th cavity as a function of the dimensionless coupling strength λ across the NP-SR phase transition of (**a**) first-order $\gamma = 0.1$, and (**b**) second-order $\gamma = 1.5$. θ is kept fixed at $2\pi/3 > \theta_c$. $\langle h_n \rangle$ is a function of the dimensionless coupling strength λ across the NP-CSR phase transition of (**c**) first-order $\gamma = 0.1$, and (**d**) second-order $\gamma = 1.5$. θ is kept fixed at $\pi/3 < \theta_c$

Availability of data and materials
All data underlying the results are available from the authors upon reasonable request.

Declarations

Competing interests
The authors declare no competing interests.

Author contribution
YYZ and HP supervised the whole project, GJC, DFP and TD performed both the analytic and numerical calculations. All authors read and approved the final manuscript.

Publisher's Note
Springer Nature remains neutral with regard to jurisdictional claims in published maps and institutional affiliations.

References
1. Greentree AD, Tahan C, Cole JH, Hollenberg LC (2006) Quantum phase transitions of light. Nat Phys 2(12):856–861
2. Hartmann MJ, Brandao FG, Plenio MB (2006) Strongly interacting polaritons in coupled arrays of cavities. Nat Phys 2(12):849–855
3. Zhu C, Ping L, Yang Y, Agarwal GS (2020) Squeezed light induced symmetry breaking superradiant phase transition. Phys Rev Lett 124(7):073602
4. Felicetti S, Le Boité A (2020) Universal spectral features of ultrastrongly coupled systems. Phys Rev Lett 124(4):040404
5. Bloch I, Dalibard J, Zwerger W (2008) Many-body physics with ultracold gases. Rev Mod Phys 80(3):885
6. Cai M-L, Liu Z-D, Zhao W-D, Wu Y-K, Mei Q-X, Jiang Y, He L, Zhang X, Zhou Z-C, Duan L-M (2021) Observation of a quantum phase transition in the quantum Rabi model with a single trapped ion. Nat Commun 12(1):1–8
7. Chen X, Wu Z, Jiang M, Lü X-Y, Peng X, Du J (2021) Experimental quantum simulation of superradiant phase transition beyond no-go theorem via antisqueezing. Nat Commun 12(1):1–8
8. Griffiths RB (1975) Phase diagrams and higher-order critical points. Phys Rev B 12:345–355
9. Chang TS, Hankey A, Stanley HE (1973) Generalized scaling hypothesis in multicomponent systems. I. Classification of critical points by order and scaling at tricritical points. Phys Rev B 8:346–364
10. Riedel EK (1972) Scaling approach to tricritical phase transitions. Phys Rev Lett 28:675–678
11. Henkel M (2013) Conformal invariance and critical phenomena
12. Xu Y, Pu H (2019) Emergent universality in a quantum tricritical Dicke model. Phys Rev Lett 122:193201
13. Yin S, Jian S-K, Yao H (2018) Chiral tricritical point: a new universality class in Dirac systems. Phys Rev Lett 120:215702
14. Belitz D, Kirkpatrick TR (2017) Quantum triple point and quantum critical end points in metallic magnets. Phys Rev Lett 119:267202
15. Friedemann S, Duncan WJ, Hirschberger M, Bauer TW, Küchler R, Neubauer A, Brando M, Pfleiderer C, Grosche FM (2018) Quantum tricritical points in nbfe2. Nat Phys 14(1):62–67
16. Kaluarachchi US, Taufour V, Bud'ko SL, Canfield PC (2018) Quantum tricritical point in the temperature-pressure-magnetic field phase diagram of $cetige_3$. Phys Rev B 97:045139
17. Wu F, Guo CY, Chen Y, Su H, Wang A, Smidman M, Yuan HQ (2019) Magnetic field induced antiferromagnetic tricritical points in Ce_2Sb and Ce_2Bi. Phys Rev B 99:064419
18. Xu Y, Fallas Padilla D, Pu H (2021) Multicriticality and quantum fluctuation in a generalized Dicke model. Phys Rev A 104:043708
19. Dicke RH (1954) Coherence in spontaneous radiation processes. Phys Rev 93:99–110
20. Lambert N, Emary C, Brandes T (2004) Entanglement and the phase transition in single-mode superradiance. Phys Rev Lett 92:073602
21. Chen Q-H, Zhang Y-Y, Liu T, Wang K-L (2008) Numerically exact solution to the finite-size Dicke model. Phys Rev A 78:051801
22. Chen X-Y, Zhang Y-Y (2018) Finite-size scaling analysis in the two-photon Dicke model. Phys Rev A 97:053821
23. Baumann K, Guerlin C, Brennecke F, Esslinger T (2010) Dicke quantum phase transition with a superfluid gas in an optical cavity. Nature 464(7293):1301–1306
24. Nagy D, Kónya G, Szirmai G, Domokos P (2010) Dicke-model phase transition in the quantum motion of a Bose-Einstein condensate in an optical cavity. Phys Rev Lett 104:130401
25. Roushan P, Neill C, Megrant A, Chen Y, Babbush R, Barends R, Campbell B, Chen Z, Chiaro B, Dunsworth A et al (2017) Chiral ground-state currents of interacting photons in a synthetic magnetic field. Nat Phys 13(2):146–151
26. Zhang Y-Y, Hu Z-X, Fu L, Luo H-G, Pu H, Zhang X-F et al (2021) Quantum phases in a quantum Rabi triangle. Phys Rev Lett 127(6):063602
27. Hayward AL, Martin AM, Greentree AD (2012) Fractional quantum Hall physics in jaynes-cummings-Hubbard lattices. Phys Rev Lett 108(22):223602
28. Hayward AL, Martin AM (2016) Superfluid-Mott transitions and vortices in the jaynes-cummings-Hubbard lattices with time-reversal-symmetry breaking. Phys Rev A 93(2):023828
29. Noh C, Angelakis DG (2016) Quantum simulations and many-body physics with light. Rep Prog Phys 80(1):016401
30. Lin Y-J, Compton RL, Jiménez-García K, Porto JV, Spielman IB (2009) Synthetic magnetic fields for ultracold neutral atoms. Nature 462(7273):628–632
31. Dalibard J, Gerbier F, Juzeli ūnas G, Öhberg P (2011) Colloquium: artificial gauge potentials for neutral atoms. Rev Mod Phys 83:1523–1543
32. Cao H, Wang Q, Fu L-B (2014) Interaction effects in a quantum simulation of classical magnetism with artificial gauge potential. Phys Rev A 89:013610
33. Umucal ılar RO, Carusotto I (2012) Fractional quantum Hall states of photons in an array of dissipative coupled cavities. Phys Rev Lett 108:206809
34. Wang D-W, Cai H, Liu R-B, Scully MO (2016) Mesoscopic superposition states generated by synthetic spin-orbit interaction in Fock-state lattices. Phys Rev Lett 116:220502
35. Han Cai D-WW (2021) Topological phases of quantized light. Nat Sci Rev 8:196
36. Bloch I, Dalibard J, Nascimbene S (2012) Quantum simulations with ultracold quantum gases. Nat Phys 8(4):267–276
37. Chang TS, Hankey A, Stanley HE (1973) Generalized scaling hypothesis in multicomponent systems. I. Classification of critical points by order and scaling at tricritical points. Phys Rev B 8:346–364
38. Fallas Padilla D, Pu H, Cheng G-J, Zhang Y-Y (2022) Understanding the quantum Rabi ring using analogies to quantum magnetism. Phys Rev Lett 129:183602
39. Zhao J, Hwang M-J (2022) Frustrated superradiant phase transition. Phys Rev Lett 128(16):163601